Energetics of M_2 Barotropic to Baroclinic tidal conversion at the Hawaiian Islands

G. S. Carter and M. A. Merrifield
JIMAR and Department of Oceanography, University of Hawaii, Honolulu, Hawaii, USA

J. Becker
Department of Geology and Geophysics, University of Hawaii, Honolulu, Hawaii, USA

K. Katsumata
IORGC, JAMSTEC, Yokosuka, Japan

M. C. Gregg
Applied Physics Laboratory, University of Washington, Seattle, USA

Y. L. Firing
Scripps Institution of Oceanography, La Jolla, California, USA

ABSTRACT

A high-resolution primitive equation model simulation is used to form an energy budget for the principal semidiurnal tide (M_2) over a region of the Hawaiian Ridge from Niihau to Maui. This region includes the Kaena Ridge, one of the three main internal tide generation sites along the Hawaiian Ridge and the main study site of the Hawaii Ocean Mixing Experiment. The one-hundredth of a degree horizontal resolution simulation has a high level of skill when compared to satellite and in-situ sealevel observations, moored ADCP currents, and notably reasonable agreement with microstructure data. Barotropic and baroclinic energy equations are derived from the model's sigma coordinate governing equations, and evaluated from the model simulation to form a energy budget. The M_2 barotropic tide loses 2.7 GW of energy over our study region. Of this 163 MW (6%) is dissipated by bottom friction and 2.3 GW (85%) is converted into internal tides. Internal tide generation primarily occurs along the flanks of the Kaena Ridge, and south of Niihau and Kauai. The majority of the baroclinic energy (1.7 GW) is radiated out of the model domain, while 0.45 GW is dissipated close to the generation regions. We find that the modeled baroclinic dissipation within the 1000 m isobath for the Kaena Ridge agrees to within a factor of two with the area weighted dissipation from 313 microstructure profiles. Topographic resolution is important, with the present 0.01° resolution model resulting in 20% more barotropic to baroclinic conversion compared to when the same analysis is performed on a 4 km resolution simulation. A simple extrapolation of our results to the entire Hawaiian Ridge is in qualitative agreement with recent estimates based on satellite altimetry data.

1 Introduction

Assimilation of satellite observations has shown that a significant fraction (~1/3) of barotropic (surface) tidal energy is lost in the open-ocean (Egbert and Ray, 2000, 2001), rather than to bottom friction in shallow marginal seas. This has led to a resurgence of interest in internal tides, as a mechanism for transferring this energy into the internal wave spectrum and subsequently to dissipation. Global simulations by Simmons et al. (2004) suggest that 75% of the open-ocean generation of internal tides occurs

[0]*Corresponding author address:* Dr. Glenn Carter, JIMAR. University of Hawaii. 1000 Pope Road, MSB 312. Honolulu HI 96822. gscarter@hawaii.edu

at 20 locations of rough topography, accounting for only ∼10% of the area of the ocean floor.

The Hawaii Ocean Mixing Experiment (HOME, Rudnick et al., 2003; Pinkel and Rudnick, 2006) investigated the conversion of barotropic to baroclinic tides at steep topography, as well as the associated diapycnal mixing. The focus on the Hawaiian Archipelago was motivated by the dominant M_2 tide propagating perpendicular to the topography, model estimates of 15–20 GW of M_2 barotropic tidal dissipation in the region (Egbert and Ray, 2001; Zaron and Egbert, 2006a), and observations of low-mode, semidiurnal baroclinic tides radiating from the Hawaiian Ridge (Chiswell, 1994; Dushaw et al., 1995; Ray and Mitchum, 1996, 1997). Numerical model studies of barotropic to baroclinic tidal conversion which focused on, or encompassed, Hawaii include Kang et al. (2000), Merrifield et al. (2001), Niwa and Hibiya (2001), Merrifield and Holloway (2002), and Simmons et al. (2004).

One of the goals of HOME was to develop an energy budget. Rudnick et al. (2003) presented a preliminary M_2 budget for the entire Hawaiian Ridge, consisting of 20 ± 6 GW lost from the surface M_2 tide (from Egbert and Ray, 2001), 10 ± 5 GW radiating outward at the 4000 m isobath as internal tides (from Merrifield and Holloway, 2002), and 10 GW of local dissipation. Although this budget 'approaches closure', it contains a number of possible weaknesses including: the Egbert and Ray (2001) and Merrifield and Holloway (2002) models having different domains, both models having coarse (≥4 km) resolution, the magnitude of barotropic to baroclinic conversion was not estimated, and that a more detailed analysis of the microstructure data reduced the estimate of local dissipation to 3 ± 1.5 GW (Klymak et al., 2006).

The focus of this current work is to develop a M_2 energy budget from a single simulation that partitions energy lost from the barotropic tide amongst barotropic and baroclinic processes. We present an one-hundredth of a degree (∼1 km) resolution simulation of the M_2 tide over a subregion of the Hawaiian Ridge (Section 2). A subregion is used primarily because of computational constraints, although much of the ridge still has not been mapped with multibeam surveys. The model output is validated against satellite and in-situ sealevel measurements, velocities from two moorings, as well as microstructure observations. To calculate the energy budget we derive barotropic and baroclinic energy equations from the model's governing equations (Section 3 and Appendix A). The energy budget presented in Section 4 shows that of the 2.7 GW lost from the barotropic tide, 2.3 GW is converted into internal tides and the majority of that baroclinic energy radiates out of the model domain. Section 5 revisits some of the findings of Merrifield and Holloway (2002), and shows that by using 4 km resolution topography and equating conversion to baroclinic flux divergence conversion is underestimated by ∼40% when compared to the present 1 km resolution simulation. Finally, our findings are summarized in Section 6.

2 Numerical simulation

2.1 Model setup

For this study we use the Princeton Ocean Model (POM), a three-dimensional, nonlinear, free-surface, finite difference, primitive equation model (Blumberg and Mellor, 1987). For computational efficiency, the model calculates the fast moving surface gravity waves separately from the internal structure, using a technique known as mode, or time, splitting. POM has been used for a number of previous studies of baroclinic tidal processes over idealized (e.g., Holloway and Merrifield, 1999; Johnston and Merrifield, 2003) and realistic topography (e.g., Cummins and Oey, 1997; Merrifield et al., 2001; Niwa and Hibiya, 2001; Merrifield and Holloway, 2002; Johnston et al., 2003).

POM uses the hydrostatic approximation, wherein the pressure is simply related to the weight of the water-column. This is valid as long as the horizontal scales of motion are much greater than the vertical scales (Hodges et al., 2006; Mahadevan, 2006). Internal tides typically meet this criterion, although exceptions include wave breaking and steepening into highly nonlinear (solitary) waves. Venayagamoorthy and Fringer (2005) found that in a bolus [a high (∼2:1) aspect-ratio, self-advecting, vortex core] the nonhydrostatic pressure was 37% of the total pressure. With sufficient horizontal resolution a hydrostatic model can identify the presence of such features but cannot accurately describe them (Holloway et al., 1999; Hodges et al., 2006), lacking the dispersive (nonhydrostatic) processes hydrostatic models tend to overestimate the steepness of the features (Hodges et al., 2006). When comparing hydrostatic and nonhydrostatic simulations, Mahadevan (2006) found it was difficult to identify the effect of the nonhydrostatic term at a horizontal resolution of 1 km.

The Mellor and Yamada (1982) level 2.5, second moment turbulence closure scheme (MY2.5) is used by POM to calculate the vertical eddy diffusivities. This k–l (turbulent kinetic energy – mixing length) submodel has be used extensively for a range of applications (over 1650 citations to date[1]), including the internal tide studies listed above. It should be noted, that this submodel was developed for application to atmospheric and oceanic boundary

[1] According to the Web of Science database.

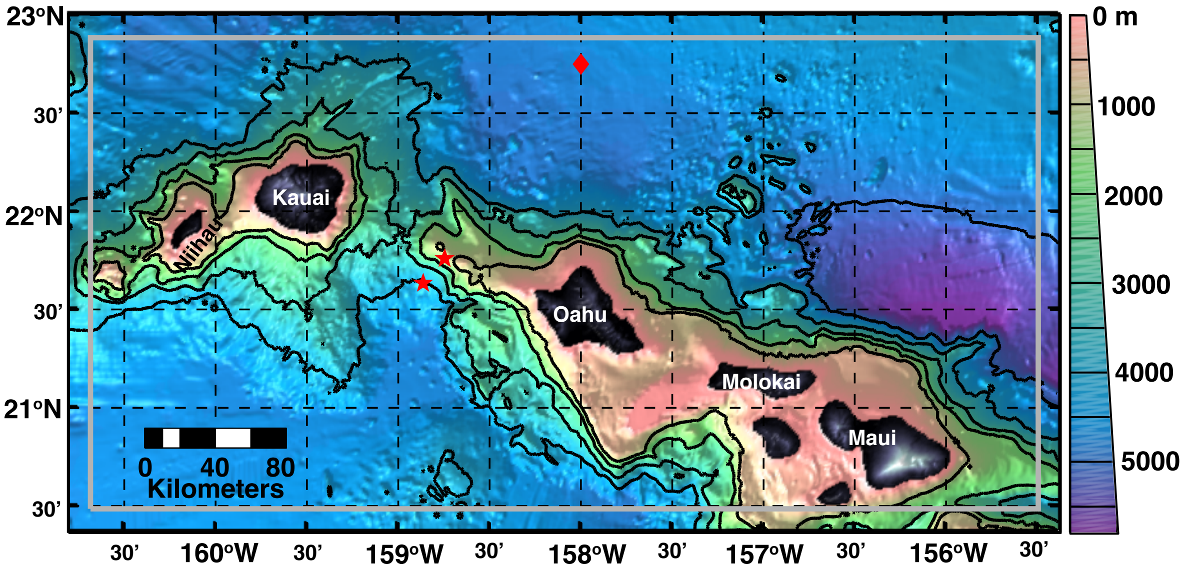

Figure 1: Bathymetric map of the model domain, horizontal resolution is one-hundredth of a degree. Contour interval is 1000 m. The gray box gives the subdomain over which the energy analysis integrations are performed. The northernmost star is the location of the A2 mooring (158° 44.75′W, 21° 45.55′N), and the more southern star is the location of the C2 mooring (158° 51.80′W, 21° 38.02′N). The diamond marks the location of Station ALOHA (158°W, 22° 45′N).

layers, and does not explicitly include the wave-wave interaction dynamics expected to dominant the dissipation of internal tide energy. Warner et al. (2005) found that MY2.5 underestimated mixing in steady barotropic and estuarine flows, but overestimated mixing in wind-driven mixed layer deepening study. We find that the combination of MY2.5 and Smagorinsky horizontal diffusivity, gives reasonable agreement with microstructure observations (Section 4.3). Finally, a quadratic bottom friction is used in POM with a logarithmic layer formulation for the coefficient (Mellor, 2004).

The simulation domain extends from 20° 21.8′N 160° 48.3′W to 23° 0.3′N 155° 22.5′W, i.e., the main Hawaiian Islands excluding the Big Island (Fig. 1). The model grid is derived from multibeam survey data, and has a horizontal spacing of one-hundredth of a degree (1111.9 m in latitude, and 1023.5–1042.4 m in longitude), with 61 sigma levels spaced evenly in the vertical. The stratification is specified using time-averaged temperature and salinity profiles obtained over 10 years at Station ALOHA, the Hawaii Ocean Time Series (HOT) site located 100 km north of Oahu (Fig. 1). This background stratification is horizontally uniform throughout the domain. Carter et al. (2006) and Klymak et al. (2006) found little variation outside the surface layer in stratification observed over the Hawaii Ridge. Surface buoyancy and momentum fluxes are set to zero, but the background stratification is preserved because neither horizontal nor vertical diffusivity is applied to temperature and salinity (i.e., these fields are simply advected).

The model is forced at the lateral boundaries using the Flather condition (Flather, 1976; Carter and Merrifield, 2007) with M_2 tidal elevation and barotropic velocity from the Hawaii region TPXO6.2 inverse model (Egbert, 1997; Egbert and Ray, 2001; Egbert and Erofeeva, 2002). Following Carter and Merrifield (2007), the baroclinic velocity fluctuations and isopycnal displacements are relaxed to zero over a 10-cell wide region. They show that this modified relaxation scheme does not reflect energy even when a range of internal tide modes are present.

The simulations are run for 18 tidal cycles (9.3 days) from a quiescent, horizontally uniform state. Over the last six tidal cycles (3.1 days) single value deposition (SVD) analysis is performed to obtain barotropic (depth averaged) and baroclinic (total minus depth-averaged[2]) har-

[2]Defining the baroclinic currents this way neglects bottom boundary layer friction. Cummins and Oey (1997) used an unstratified simulation to remove the bottom friction component from the true baroclinic tidal signal and found the results to be virtually identical to using the 'total minus depth-averaged' definition. We expect this to also hold for our domain as bottom friction should be most pronounced in shallow water, and unlike Cummins and Oey (1997) there is no significant continental shelf within our domain.

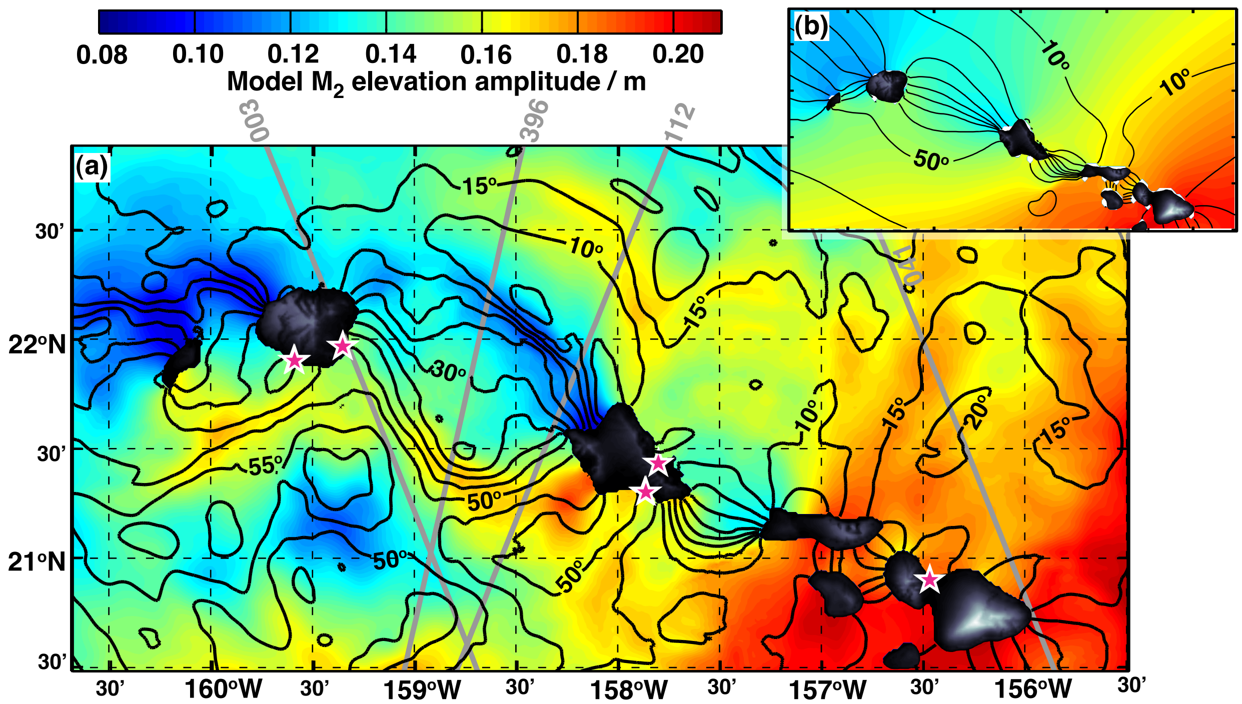

Figure 2: M$_2$ cotidal plots from (a) our baroclinic POM model run, and (b) the 2D TPXO inverse model. The amplitude color range is the same in both panels. Greenwich phases are plotted with a contour interval of 5°. The five stars mark the location of long-term NOAA sealevel gauges: Port Allen on the south shore of Kauai; Nawiliwili on the east shore of Kauai; Honolulu on the south shore of Oahu; Mokuoloe on the northeast shore of Oahu; and Kahului on the north shore of Maui. The gray lines mark satellite altimetry tracks. Tracks 003, 112, and 041 are TOPEX-Poseidon. Track 396 is the European Space agency's ERS satellite.

monic amplitudes and phases. Also the barotropic and baroclinic energy equations [equations (4) and (5) in Section 3] are averaged over the same six tidal cycles.

2.2 Model validation

Using sealevel data, Larson (1977) noted a 46° (1.5 hour) M$_2$ phase shift across the island of Oahu, between Mokuoloe and Honolulu. Ray and Mitchum (1997) argued that most of this phase difference is likely due to the presence of the shallower topography along the Hawaiian Ridge, with additional contributions from the baroclinic tides. This is confirmed by comparing cotidal plots of our baroclinic (Fig. 2a) and the TPXO barotropic (Fig. 2b) simulations. Although most of the phase difference is in the barotropic field, the inclusion of baroclinic tides adds significant small scale variability. The baroclinic tide has a noticeable effect on the amplitude around Oahu and Kauai. In particular, the amplitudes are reduced on the north shore of Oahu and increased on the western coast compared to the barotropic calculation.

Table 1: Comparison of M$_2$ surface amplitudes and phases between the model and sealevel gauges. The stations are part of NOAA's water level observation network. Phase is relative to the equilibrium tide at Greenwich, E is the RMS error defined in (1).

Station	Model		Obs.		E
	A_m. (m)	G_m (°)	A_o. (m)	G_o (°)	(m)
Port Allen	0.152	40.5	0.159	44.1	0.009
Nawiliwili	0.147	45.1	0.149	48.3	0.006
Honolulu	0.165	57.0	0.178	59.5	0.010
Mokuoloe	0.151	11.2	0.161	13.9	0.009
Kahului	0.183	14.5	0.187	8.6	0.014

A first check on the model skill is provided by comparing the modeled surface elevation amplitude and phase with coastal sealevel observations (Table 1). NOAA's Center for Operational Oceanographic Products and Services (CO-OPS) maintains long-term, quality controlled,

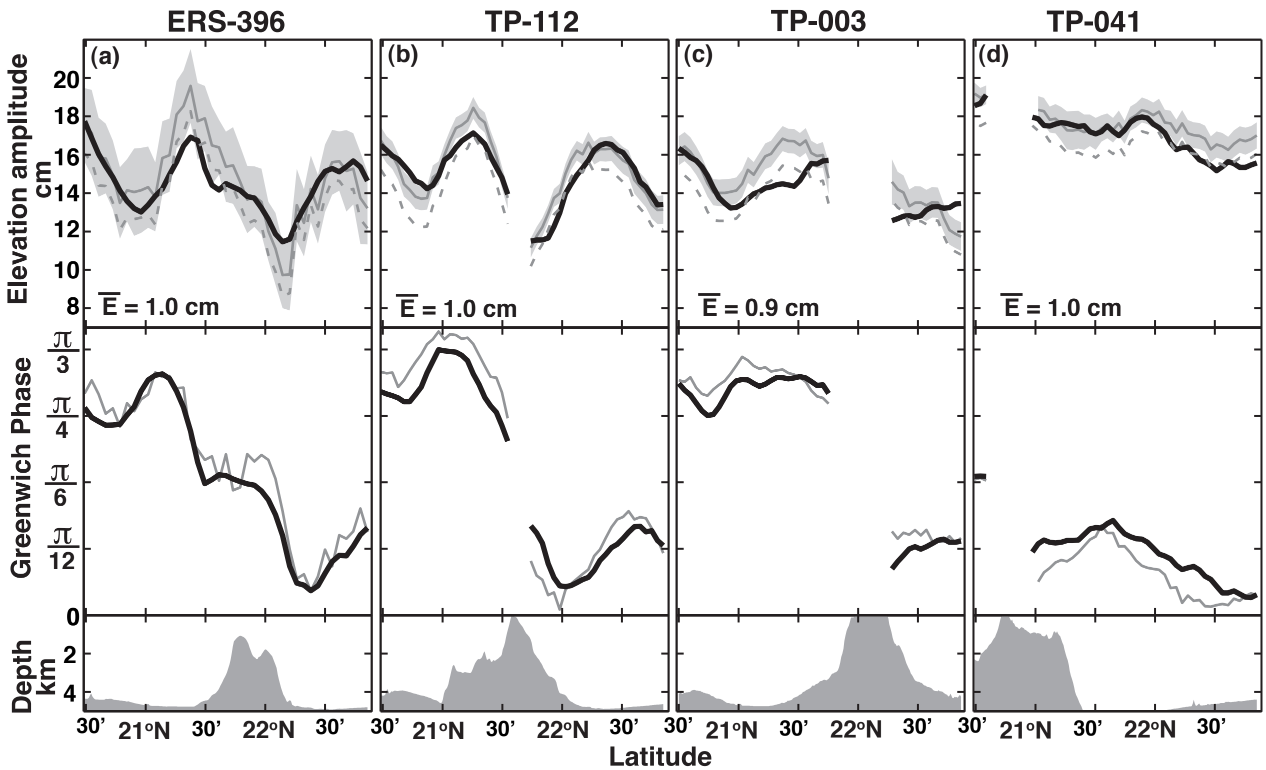

Figure 3: Comparison of total M$_2$ surface elevation (barotropic plus baroclinic) from the model (black line) and from satellite altimetry (gray line). The location of the tracks are shown as gray lines in Fig. 2a. In the amplitude panels, the gray shading shows ± 1 standard error for the satellite amplitude measurements, and the dashed gray line is the satellite altimetry without the load tide correction.

records from gauges at Port Allen, Nawiliwili, Honolulu, Mokuoloe, and Kahului (location shown with stars in Fig. 2a). The data and harmonic constants are available online. Following Cummins and Oey (1997) a quantitative comparison is given using an absolute RMS error,

$$E = \sqrt{\frac{1}{2}(A_o^2 + A_m^2) - A_o A_m \cos(G_o - G_m)}, \quad (1)$$

where subscript o and m denoted observed and modeled amplitudes (A) and phases (G). The model and observations are in good agreement, with three sites having $E < 9$ mm. The Honolulu and Mokuoloe gauges, where amplitude differences are 10–13 mm, are in Honolulu Harbor and Kaneohe Bay, respectively, which are not fully resolved by the model. The largest RMS error at Kahului is due to a 5.9° ($\sim$12 min) phase difference, which presumably is due to the narrow harbor entrance.

The baroclinic cotidal plot (Fig. 2a) shows that the surface elevation amplitudes and phases, particularly between Oahu and Kauai, are influenced by the surface bounce of the baroclinic tide. The yellow-red band is where the near surface baroclinic displacement is in-phase with the barotropic tide, resulting in increased elevation, and conversely the dark blue bands are out-of-phase. To evaluate how well we have simulated the surface elevation away from land, a comparison is made to the along-track M$_2$ fits of satellite altimetry data (Fig. 3). In addition to the three TOPEX-Poseidon tracks (TP-003, TP-112, and TP-041) that cross the domain, we also consider data from the European Space Agency's ERS satellite (track 396) which goes though the middle of the Kauai Channel. The positions of the tracks are shown as gray lines in Fig. 2a. Overall, there is very good agreement in both amplitude and phase between our simulation and the satellite altimetry. Often the model lies within one standard error of the satellite data (Fig. 3, gray shading). The average RMS error along each track, $\overline{E} = n^{-1}\sum_n E$, ranges from 0.9 to 1.0 cm. The largest amplitude differences are on the order of 2 cm and occur at the first surface bounce along the ERS-396 track, and around Kauai (TP-003).

This POM simulation, like the TPXO model from which the boundary conditions are derived, calculates the

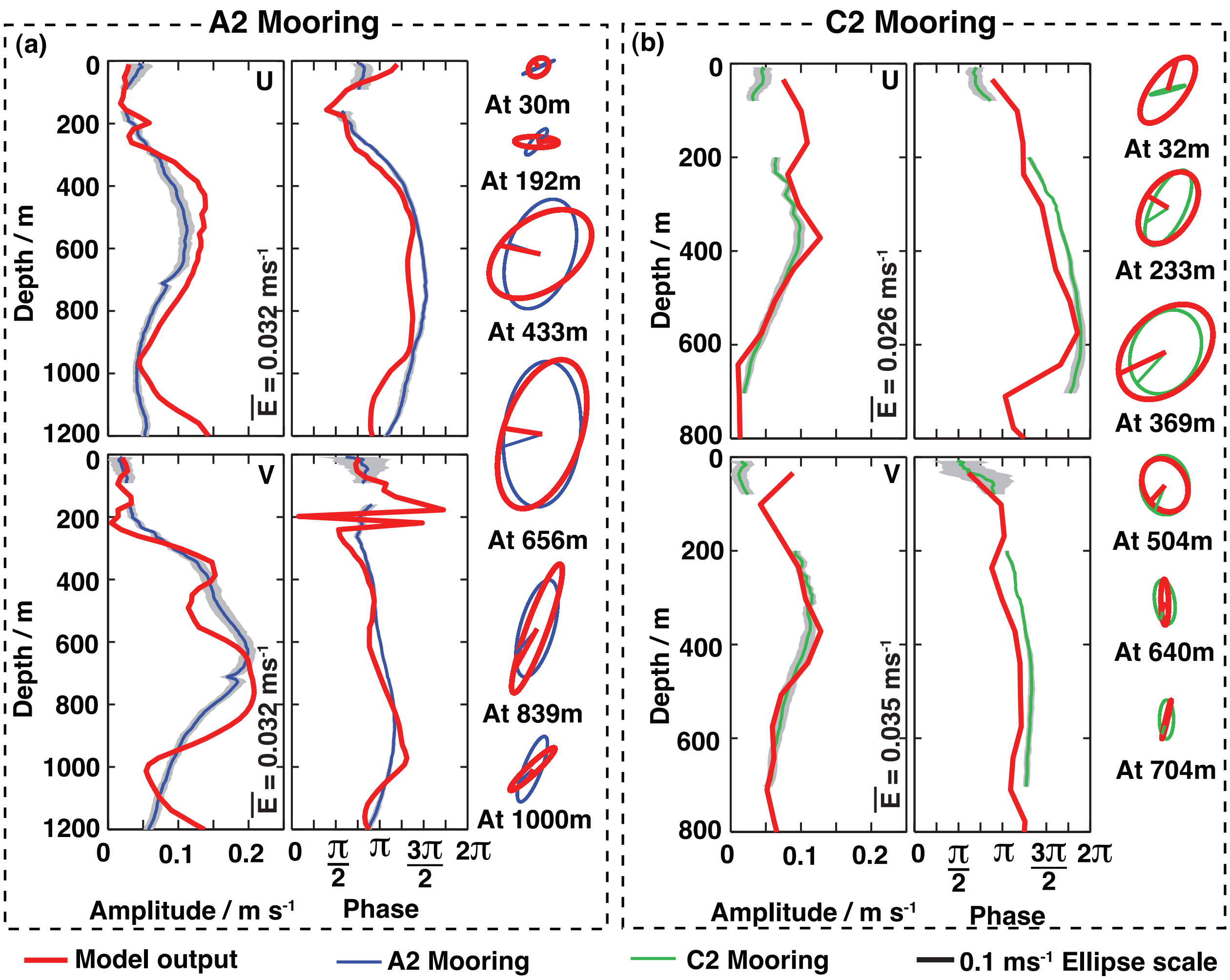

Figure 4: Comparison of M$_2$ harmonic fits from the model and 5 months of moored ADCP data. (a) A2 mooring on the edge of the ridge crest; (b) C2 mooring south of the ridge. Ellipses are from depths where the model velocities were nearly collocated with ADCP observation.

height of the ocean surface relative to the seabed. The satellite altimetry, however, gives the surface height relative to a reference geoid. The difference between these two measurements is the 'load tide', the deformation of the solid earth due to the weight of the water above it. In the above comparisons, the satellite observations have had the load tide added using the TPXO6.2_load model. The dashed lines in the amplitude panels show the original (without load tide) satellite elevations. Inclusion of the load tide reduces $\overline{E}$ for TP-041 by 54%; for TP-112 by 26% and ERS-396 by 2%; but increases $\overline{E}$ for TP-003 by 10%. This is the first time, to our knowledge, that a process tide model has been shown to be accurate enough to require the load tide correction when validating to satellite data.

An intensive field experiment, the HOME Nearfield, which was conducted at Kaena Ridge from 2001 to 2003, resulted in detailed observations of the currents and mixing patterns. As a check on the validity of the model, we compare model output to M$_2$ harmonic fits from two moorings. One mooring, A2, was located on the southern edge of Kaena Ridge (Fig. 1, northern star) with three ADCPs giving coverage of most of the water-column. The second mooring, C2, was located south of the ridge in ∼4000 m water depth (Fig. 1, southern star) with coverage only in the upper 700 m.

The magnitudes and vertical structure of the model amplitudes and phases agree well, for the most part, with the mooring observations (Fig. 4). $\overline{E}$ range from 0.026 to 0.035 m s^{-1}. The largest amplitude differences are near the seafloor in A2 (Fig. 4a), where the model overpredicts both the u and v currents. An across-ridge section (not shown) indicates that the model predicts the formation of a near-bed downward propagating beam at A2. Such beams have been observed elsewhere on the Kaena Ridge (e.g., Nash et al., 2006; Aucan et al., 2006), but their formation is dependent on the criticality of the local slope (Balmforth et al., 2002; Garrett and Kunze, 2007). It is possible that near A2 the 0.01° resolution topography is closer to critical than the actual topography.

At mooring C2, the model predicts a surface intensification in v-velocity which is not seen in the observations (Fig. 4b). Important near-surface forcing processes such as the wind and mesoscale activity are not included in this simulation, and could easily alter the surface velocities. High-frequency radar observations at the Kaena Ridge, taken as part of HOME, show that the M_2 surface velocity pattern predicted by the model is usually masked or altered by mesoscale processes (Chavanne, 2007).

Current ellipses at depths where the model levels are nearly collocated with the ADCP measurements show good agreement at subsurface depths (Fig. 4). Near the surface, flows at both moorings are more rectilinear than predicted by the model.

Our ability to verify the simulation with the suite of observations described above gives us a high level of confidence in the model's ability to simulate the M_2 internal tide around the steep topography of the Hawaiian Islands. Including the baroclinic tide improves the prediction of the water level around the Hawaiian Islands. The rms errors from the along-track satellite data ($\overline{E} \approx 1.0$ cm) are approximately one-third those for the barotropic M_2 TPXO model, which have been estimated to be less than 3 cm (Simmons et al., 2004).

2.3 Modeled internal tide structure

Although the focus of this work is on the energetics, it is constructive to briefly examine the structure of the internal tide generated at the Kaena Ridge. A transect across the ridge shows a complex vertical displacement and baroclinic current structure (Fig. 5a,c). Beam-like features emanate from the flanks of the ridge, as well as from discontinuities deeper in the water column. This transect was chosen to pass through two stations occupied as part of the Hawaii Ocean Timeseries experiment, including Station ALOHA where Chiswell (1994) observed internal tides from repeat hydrographic surveys. The structure is shown during maximum north-northeastward barotropic current (Fig. 5a), and the quadrature structure 3 hours later during barotropic slack tide (Fig. 5c). Peak baroclinic currents (0.24 m s^{-1}) and displacements (92 m) are found along the tidal beams that originate on both sides of the ridge. During both plotted phases the displacement is upward on the south side and downward on the north side of the ridge. When the barotropic current slackens to near zero, 180° phase shifts of the baroclinic current occur in the beam, consistent with classic analytic descriptions of tidal beams (e.g., Rattray et al., 1969). The beams are more focused during maximum across-ridge barotropic flow than at slack flow.

The baroclinic energy flux (not shown) follows the same three main pathways seen in the vertical displacement: up and away from the ridge leading to surface bounces ∼40 km on either side of the crest; up and over the top of the ridge, with beams crossing over the crest resulting in weaker fluxes; and down and away with some contact with the bottom along the near and supercritical slope. The crossing beams over the crest of the ridge have been described as a quasi-standing wave by Nash et al. (2006) and Carter et al. (2006). The downward-propagating beams have been examined in the context of near-boundary mixing by Aucan et al. (2006) and Aucan and Merrifield (2007).

The horizontal variability in the baroclinic structure can be assessed by considering the total (barotropic plus baroclinic) surface currents (Fig. 5b and d). The banding of higher velocity that parallels the ridge corresponds to the interaction of the beam with the surface mixed layer. The first surface bounce has velocities of ∼0.2 m s^{-1}. Notice that near Station Kaena this surface baroclinic current is comparable with the barotropic current over the ridge crest (Fig. 5a, blue arrows). Further west, where the ridge crest is deeper, the baroclinic surface currents associated with the surface bounce exceed the barotropic currents over the ridge crest (Fig. 5b). Overall, the strongest surface currents (up to 0.55 m s^{-1}) are barotropic and are found over the shallow Penguin Bank, southwest of Molokai.

3 Barotropic and baroclinic energy equations

To quantify how energy lost from the barotropic tide is distributed amongst barotropic and baroclinic processes, we develop and evaluate barotropic and baroclinic energy equations derived from POM's governing equations. In each equation the energy is partitioned into tendency, flux divergence, nonlinear advection, barotropic to baroclinic conversion, and dissipation. The tendency, or time varying component, would be zero for a perfectly steady state

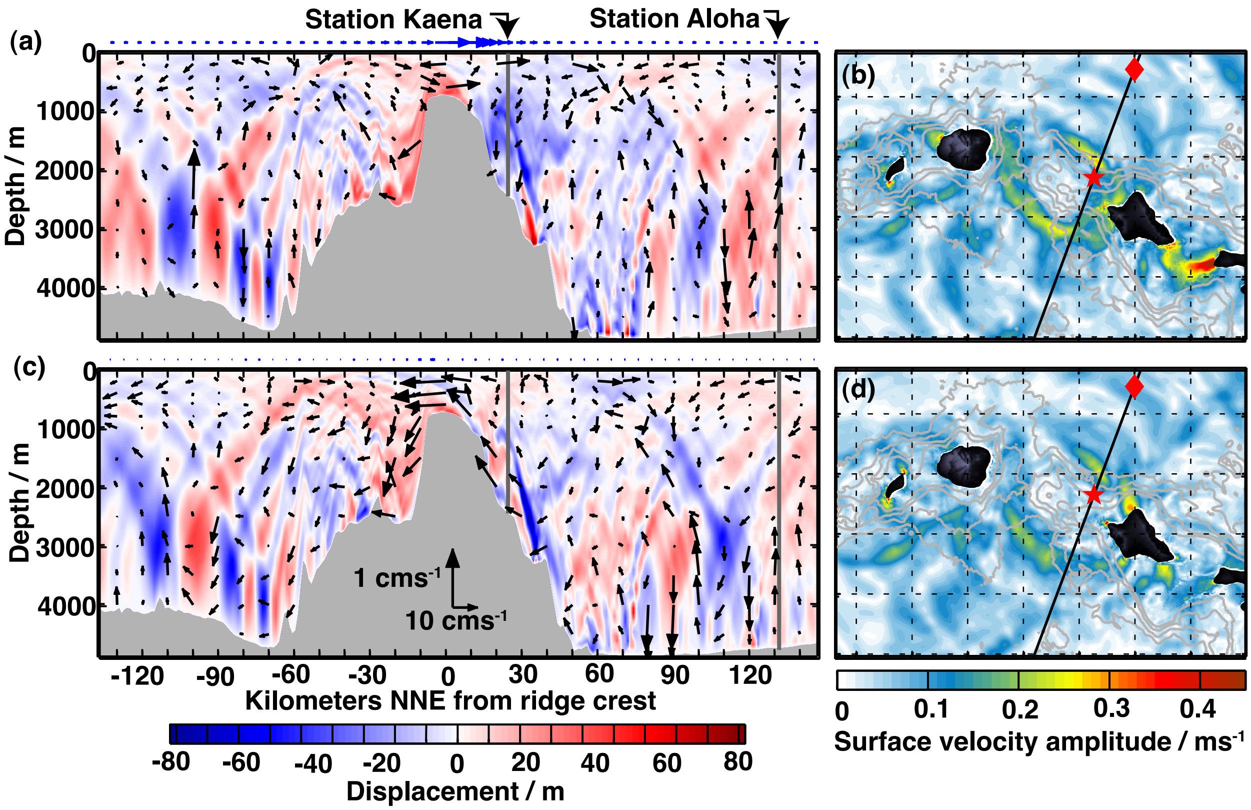

Figure 5: M$_2$ baroclinic currents (along-section) and vertical displacement on a cross-ridge section through the Hawaii Ocean Timeseries stations ALOHA and Kaena during (a) maximum north-northeast barotropic current, and (c) 90° later during slack current. The vectors at the top of the two left-hand panels are the across-ridge barotropic currents. The total surface current (barotropic plus baroclinic) for the domain west of 157°W at (b) maximum north-northeast barotropic current, and (d) 90° later during slack current. The black line shows the location of the section in (a) and (c). The diamond and star indicate the locations of Station ALOHA and Station Kaena, respectively.

solution. The conversion terms in the barotropic and baroclinic equations are derived independently, but should be numerically similar as they represent the same process. The conversion term is a sink in the barotropic equation and a source in the baroclinic.

The energy equations, like the POM momentum equations, are in terms of sigma-coordinates. The relationship between the z-coordinate and the σ-coordinate is

$$\sigma = \frac{z-\eta}{D}, \tag{2}$$

where η is the surface elevation, the seafloor is at $z = -H$, and the total depth of the water column is $D = H + \eta$. The horizontal velocity components are u, v, and ω is the across-sigma-coordinate velocity. The vertical velocity is given by

$$w = \omega + u\left(\sigma\frac{\partial D}{\partial x} + \frac{\partial \eta}{\partial x}\right) + v\left(\sigma\frac{\partial D}{\partial y} + \frac{\partial \eta}{\partial y}\right) + \sigma\frac{\partial D}{\partial t} + \frac{\partial \eta}{\partial t}. \tag{3}$$

The density is decomposed into a constant, a depth-varying, and a perturbation component (i.e., $\rho_{total} = \rho_0 + \hat{\rho}(\sigma D + \eta) + \rho(x, y, \sigma, t)$. Finally since the bottom is not necessarily flat, we define the barotropic component, denoted by an overbar ($\bar{\bullet}$), to be the vertical average. The baroclinic component, denoted by a tilde ($\tilde{\bullet}$) is then taken to be the total minus barotropic.

The barotropic energy equation in m^3 s^{-3}, with each term labeled for ease of reference, is:

$$\boxed{\text{Tendency}} \quad D\frac{\partial}{\partial t}\left(\frac{\bar{u}^2 + \bar{v}^2}{2}\right) + \frac{\partial}{\partial t}\left(g\frac{\eta^2}{2}\right)$$

$$\boxed{\nabla\cdot\text{Flux}} \quad + \frac{\partial}{\partial x}\left[D\bar{u}\left(g\eta + \frac{\bar{p}}{\rho_0}\right)\right] + \frac{\partial}{\partial y}\left[D\bar{v}\left(g\eta + \frac{\bar{p}}{\rho_0}\right)\right]$$

$$\boxed{\text{Advection}} \quad + D\bar{u}\overline{\mathcal{A}'_x} + D\bar{v}\overline{\mathcal{A}'_y}$$

$$\boxed{\text{Conversion}} \quad = -\frac{\bar{p}}{\rho_0}\frac{\partial \eta}{\partial t} + \frac{D\bar{u}}{\rho_0}\left(\frac{\partial \bar{p}}{\partial x} - \overline{g\int_\sigma^0 \left[\frac{\partial \rho}{\partial x} - \sigma'\frac{1}{D}\frac{\partial D}{\partial x}\frac{\partial \rho}{\partial \sigma'}\right] D d\sigma'}\right) + \frac{D\bar{v}}{\rho_0}\left(\frac{\partial \bar{p}}{\partial y} - \overline{g\int_\sigma^0 \left[\frac{\partial \rho}{\partial y} - \sigma'\frac{1}{D}\frac{\partial D}{\partial y}\frac{\partial \rho}{\partial \sigma'}\right] D d\sigma'}\right)$$

$$\boxed{\text{Dissipation}} \quad + D\bar{u}\left(\overline{\mathcal{D}_x} + \overline{\mathcal{F}_x}\right) + D\bar{v}\left(\overline{\mathcal{D}_y} + \overline{\mathcal{F}_y}\right). \tag{4}$$

Similarly, the depth-integrated baroclinic energy equation is:

$$\boxed{\text{Tendency}} \quad \int_{-1}^{0}\frac{\partial}{\partial t}\left(\frac{\tilde{u}^2+\tilde{v}^2}{2}\right)Dd\sigma + \int_{-1}^{0}\frac{g}{\rho_0}\left(-\frac{d\hat{\rho}}{dz}\right)^{-1}\frac{\partial}{\partial t}\frac{\rho^2}{2}Dd\sigma$$

$$\boxed{\nabla\cdot\text{Flux}} \quad + \frac{1}{\rho_0}\frac{\partial}{\partial x}\int_{-1}^{0}\tilde{u}\tilde{p}Dd\sigma + \frac{1}{\rho_0}\frac{\partial}{\partial y}\int_{-1}^{0}\tilde{v}\tilde{p}Dd\sigma$$

$$\boxed{\text{Advection}} \quad + \int_{-1}^{0}\tilde{u}\widetilde{\mathcal{A}_x}Dd\sigma + \int_{-1}^{0}\tilde{v}\widetilde{\mathcal{A}_y}Dd\sigma + \int_{-1}^{0}\frac{g}{\rho_0}\left(-\frac{d\hat{\rho}}{dz}\right)^{-1}\rho\widetilde{\mathcal{A}_\rho}Dd\sigma$$

$$\boxed{\text{Conversion}} \quad = -\int_{-1}^{0}\frac{\tilde{p}}{\rho_0}\frac{\partial \omega}{\partial \sigma}d\sigma + \int_{-1}^{0}\frac{g}{\rho_0}\rho w D d\sigma - \int_{-1}^{0}\left\{\frac{g}{\rho_0}\widetilde{\rho\sigma}\left(\tilde{u}\frac{\partial D}{\partial x} + \tilde{v}\frac{\partial D}{\partial y}\right) + \frac{g}{\rho_0}\tilde{\rho}\left(\tilde{u}\frac{\partial \eta}{\partial x} + \tilde{v}\frac{\partial \eta}{\partial y}\right)\right\}Dd\sigma$$

$$\boxed{\text{Dissipation}} \quad + \int_{-1}^{0}\tilde{u}\left(\widetilde{\mathcal{D}_x} + \widetilde{\mathcal{F}_x}\right)Dd\sigma + \int_{-1}^{0}\tilde{v}\left(\widetilde{\mathcal{D}_y} + \widetilde{\mathcal{F}_y}\right)Dd\sigma + \int_{-1}^{0}\frac{g}{\rho_0}\left(-\frac{d\hat{\rho}}{dz}\right)^{-1}\rho\left(\mathcal{D}_\rho + \mathcal{F}_\rho\right)Dd\sigma, \tag{5}$$

where g is gravitational acceleration, and p is the perturbation pressure (calculated from the perturbation density). $\mathcal{A}$, $\mathcal{D}$, and $\mathcal{F}$ denote the advection, vertical dissipation, and horizontal dissipation terms, respectively. The definition of these terms, along with the derivation of (4) and (5), are given in Appendix A. These equations are evaluated at each time step and then averaged over an integer number of tidal periods. Note that as we are only advecting temperature and salinity in this study, $\mathcal{D}_\rho \equiv \mathcal{F}_\rho \equiv 0$.

This approach differs from previous numerical studies which have evaluated energy fluxes from harmonic fits to model timeseries (e.g., Cummins and Oey, 1997; Merrifield and Holloway, 2002). Equation (5) also emphasizes the difference between the barotropic to baroclinic conversion, which directly measures the work done by the barotropic tide on the baroclinic tide, and the baroclinic flux divergence, which measures radiated baroclinic energy. Merrifield and Holloway (2002) and Di Lorenzo et al. (2006) equated conversion to baroclinic flux divergence, thereby neglecting local baroclinic dissipation. Niwa and Hibiya (2001) and Zilberman et al. (2007) calculate conversion from the harmonic fits as

$$c = \langle p'(-H).\,(\bar{\mathbf{u}}.\nabla H)\rangle_\theta\,, \tag{6}$$

where $p'(z) = \int_z^0 N^2\zeta dz' - \frac{1}{H}\int_{-H}^0\int_z^0 N^2\zeta dz' dz''$ is the perturbation pressure (Kunze et al., 2002), ζ is the isopycnal displacement, $\bar{\mathbf{u}}$ is the M$_2$ harmonic fit for the barotropic velocity, and $\langle\bullet\rangle_\theta$ indicates an average over a tidal cycle. In his figure 6, Katsumata (2006) schematically partitioned the energy into the same categories as used in (4) and (5), but he did not publish the equations. Zaron and Egbert (2006b), as part of a verification study, partition energy into reservoirs of kinetic and available potential energy.

4 Energy Analysis

4.1 Energy Balance

The terms of the barotropic and baroclinic energy equations [(4) and (5)] are averaged over the last 6 M$_2$ tidal cycles of an 18-tidal-cycle simulation. The area integrals presented in this section exclude the outer 12 cells along each boundary (160° 41.1′W, 20° 29.1′N to 155° 29.7′W, 22° 53.1′N; gray line in Fig. 1). This exclusion is conservative, as there is no evidence that the effect of the relaxation layer extends beyond its 10-cell width (Carter and Merrifield, 2007).

A total of 2.733 GW is lost from the barotropic tide within our domain (Table 2). The majority of this

Table 2: Model barotropic and baroclinic energy estimates in gigawatts (GW, 10^9 W) integrated over the subdomain shown in Fig. 1. The sign of each term is consistent with its position in equations (4) and (5). The error term is defined as the remainder after moving the terms to the left hand side of (4) or (5) and summing.

	Tendency	$\nabla\cdot$Flux	Advection	Conversion	Dissipation	Error
Barotropic	-0.006	-2.733	-0.005	-2.286	-0.163	-0.296
Baroclinic	$+0.054$	$+1.701$	$+0.016$	$+2.340$	-0.445	-0.125

barotropic flux divergence is converted into baroclinic tides (2.286 GW), with the bottom friction (barotropic dissipation term) accounting for 0.163 GW. Of the energy converted from barotropic to baroclinic, 73% radiates out of the domain as baroclinic flux ($\nabla\cdot\text{Flux}_{bc}$ = 1.701 GW). The majority of the remaining baroclinic energy is lost to dissipation within the domain (0.445 GW, 19%).

Although the simulation is forced with M_2-only, nonlinear dynamics can transfer energy to higher harmonics (M_4, $M_6, \cdots$, e.g., Lamb, 2004), or the subharmonic ($\frac{1}{2}M_2$, e.g., Carter and Gregg, 2006), or into rectified tides. In (4) and (5), energy actively undergoing a nonlinear transformation would be in the advection term, whereas the tendency term includes the time rate of change of energy at all frequencies. The tendency and nonlinear advection terms are small in both the barotropic and baroclinic equations, suggesting little energy at, or being transferred to, other constituents. As the simulation started from quiescent state, there was no 'seed' energy at other frequencies to facilitate wave-wave interactions, and therefore, it is likely the nonlinear interactions are underestimated.

The computational mode splitting technique can produce an erroneous energy source (Simmons et al., 2004; Zaron and Egbert, 2006b). Simmons et al. (2004) found that with a ratio of eight or less barotropic iterations to one baroclinic iteration the energy error was $<10\%$, which they considered to not have a qualitative impact on their analysis. Our barotropic error term is 10.8% of the flux divergence (-0.296 GW), which we attribute to the 50:1 mode split used in the present simulation. The baroclinic error is 5.3% of the conversion term, twice the difference between the two estimates of conversion (2.4%).

A 30 M_2 tidal cycle simulation was performed to check the stability of the 18 tidal cycle results. As in the 18 tidal cycle simulation, the energy analysis was performed over the last 6 tidal cycles. The flux divergence and conversion values changed by $\lesssim$1% in both the barotropic and baroclinic balances. The absolute differences in dissipation were similar, 0.01–0.03 GW, which due to their small initial values results in differences of 3–7%.

Sigma coordinate models such as POM generate erroneous currents through a pressure gradient error (e.g., Mellor et al., 1994). In this simulation we observed these zero-frequency currents to be layered throughout the water column with the layers having opposite sign, such that they cancel in the vertical integral. Being zero-frequency they are excluded from the harmonic fits, so a further check on (4) and (5) is obtained by calculating the conversion from the harmonic fits using (6). This approach gives 2.368 GW of conversion, which is larger than our baroclinic value by only 1.2%. The mean and standard deviation of the RMS differences between the barotropic model output and the corresponding harmonic time-series are [1.5, 0.8] mm, [2.0, 5.5] mm s^{-1}, [1.9, 4.8] mm s^{-1} for η, $\bar{u}$, and $\bar{v}$ respectively. Only the barotropic field time-series could be stored due to file size constraints. The largest departures from sinusoidal (RMS differences) occur near headlands on Oahu and Molokai (not shown). Therefore we conclude that non-M_2 currents, both physical (M_4, M_6,$\cdots$) and erroneous, have little effect on the regional energy balances.

4.2 Structure of baroclinic energy fields

The $\sim$2.3 GW lost to internal tides in the barotropic energy balance becomes the source term in the baroclinic balance. The barotropic to baroclinic conversion occurs mainly on both sides of the Kaena Ridge, northwest of Oahu, and south of the 1000 m isobath surrounding Kauai and Niihau (Fig. 6a). M_2 conversion is weak in the Kaiwi Channel (between Oahu and Molokai), although conversion occurs off Makapuu, the eastern tip of Oahu. Very little conversion occurs east of 157°W. Forty percent of the internal tide generation occurs between the 1000 and 2000 m isobaths, and 84% occurs over topography shallower than 3000 m (Fig. 6b).

From these generation sites, baroclinic energy radiates away from the ridge (Fig. 7). The largest fluxes are contained within two beams: one propagating northeast from the Kaena Ridge, and a southward beam formed from the interaction of the Niihau and Kaena generation sites. The broad dimensions of these beams are set by the length of the generation region, and as such similar features are

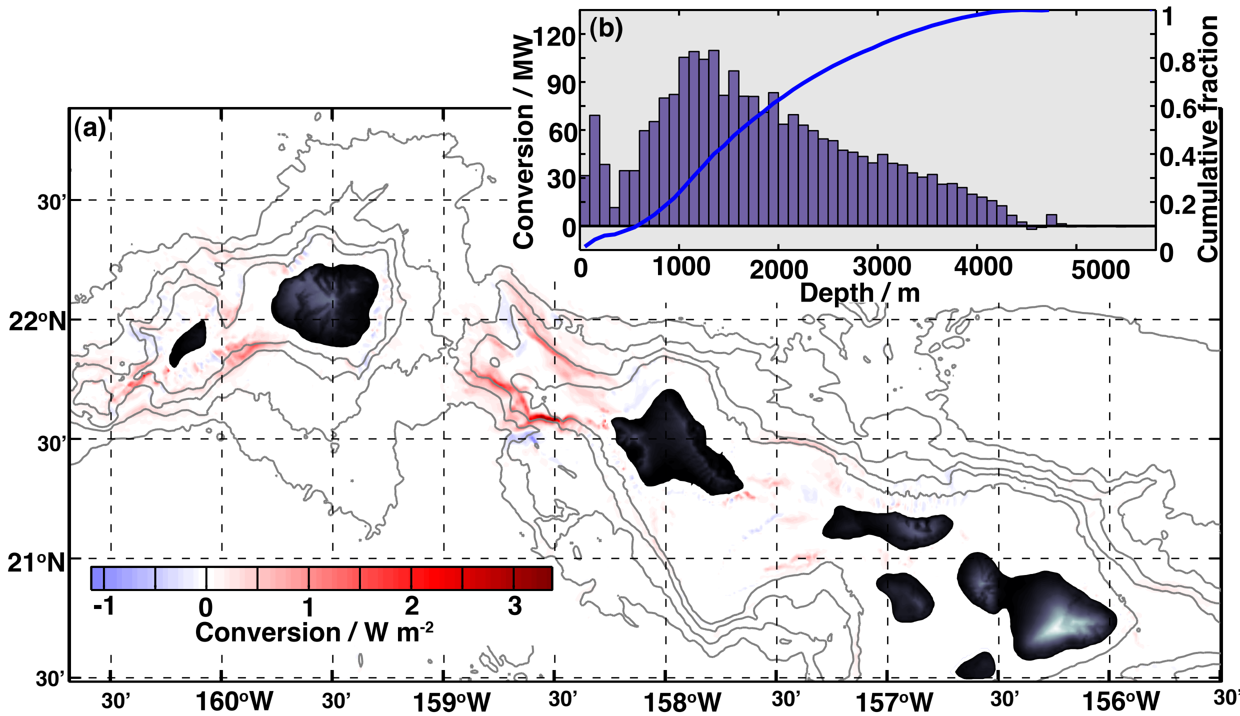

Figure 6: (a) Map of barotropic to baroclinic conversion. The sign is consistent with it being a source term in the baroclinic equation. Contour interval is 1000 m. (b) Area integral of conversion term in 100 m depth bins, and the cumulative fraction of conversion occurring in and above each depth bin.

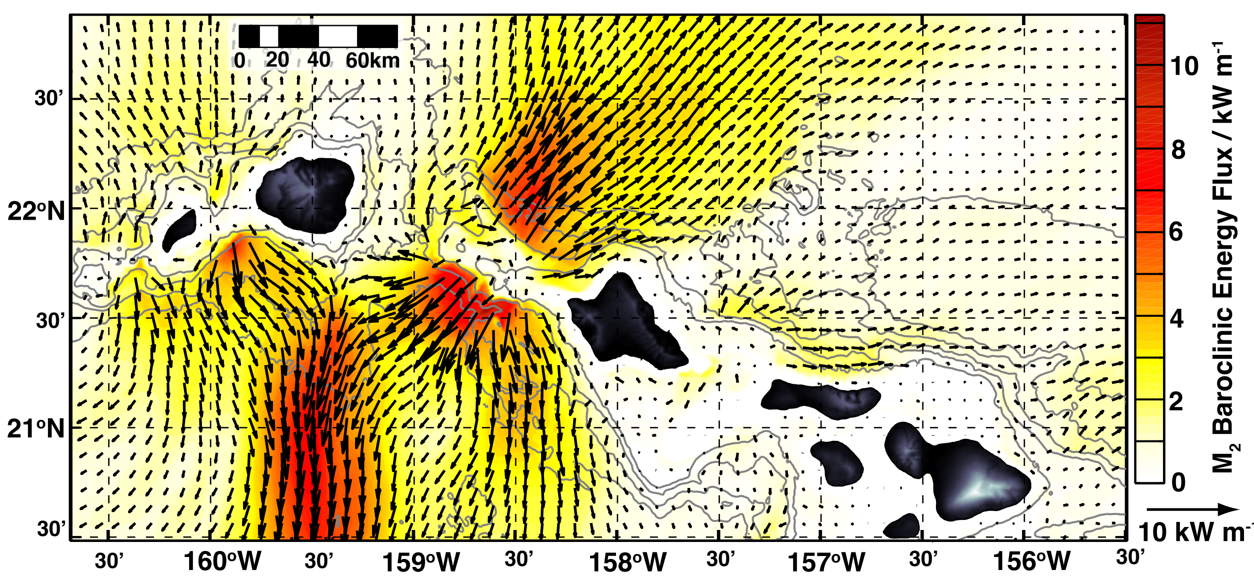

Figure 7: Depth-integrated M$_2$ baroclinic energy flux vectors. Every eighth vector in each direction has been plotted. The underlying color gives the flux magnitude. Contour interval is 1000 m.

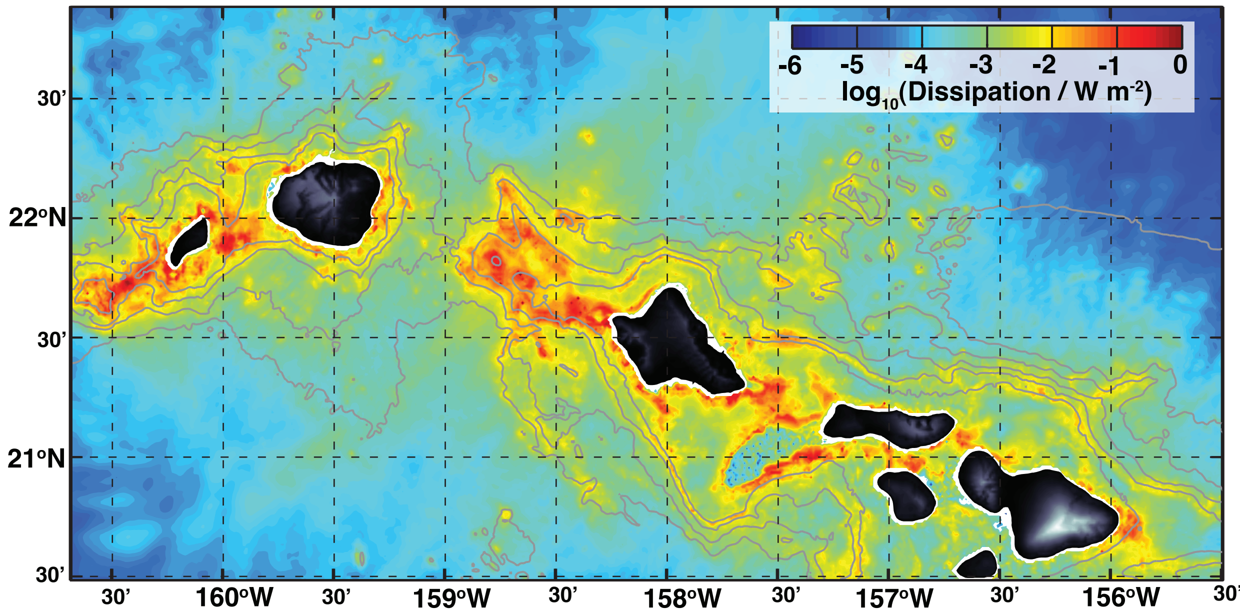

Figure 8: Map of depth integrated baroclinic dissipation from the model. This includes both vertical $\left[\int_{-1}^{0}\left(\tilde{u}\widetilde{\mathcal{D}_x}+\tilde{v}\widetilde{\mathcal{D}_y}\right)d\sigma\right]$ and horizontal $\left[\int_{-1}^{0}\left(\tilde{u}\widetilde{\mathcal{F}_x}+\tilde{v}\widetilde{\mathcal{F}_y}\right)d\sigma\right]$ contributions. As we are only advecting temperature and salinity $\mathcal{D}_\rho \equiv \mathcal{F}_\rho \equiv 0$. Contour interval is 1000 m.

seen in the coarser simulations of Merrifield and Holloway (2002) and Simmons et al. (2004). The global simulations of Simmons et al. (2004) show that in the absence of mesoscale disturbances these beams are coherent for large distances. The details and magnitude of the fluxes are, however, dependent on the slope and resolution of the topography.

Small scale structures are observed emanating from localized generation regions. A second, southward beam occurs as a result of fluxes from the near-Oahu end of Kaena Ridge being steered by the topography south of Oahu. North of Molokai there is a $\sim$30 km wide beam parallel to the isobaths, and the generation off Makapuu Point leads to baroclinic energy fluxes which are steered around the south shore of Oahu. The smooth transitions between the flux regions is likely due to the linearity of the solutions (Section 4.1), as well as low numerical noise.

The rate of turbulent baroclinic energy loss within the model is a combination of the MY2.5 submodel (κ_m) and the Smagorinsky horizontal diffusivity (A_M). These quantities enter (5) through the $\mathcal{D}_x$, $\mathcal{D}_y$, and $\mathcal{F}_x$, $\mathcal{F}_y$ terms respectively. The total amount of vertical (submodel) mixing appears to be partly dependent on how noisy the simulation is, and in our simulations the vertical mixing from the submodel is less than expected from observations. However, the combined horizontal and vertical baroclinic dissipation is consistent with the observed diapycnal mixing. From microstructure observations at a small seamount on the Kaena Ridge (158° 38.8′W, 21° 43.8′N), Carter et al. (2006) found an average turbulent dissipation rate of $\bar{\varepsilon} = 6.2 \times 10^{-8}$ W kg^{-1}. If averaged over the water column ($\bar{\varepsilon}\rho_0 D$, where D=1000 m and ρ_0=1025 kg m^{-3}), this would be $\sim 10^{-1}$ W m^{-2} similar to the modeled dissipation in that location. A more detailed comparison to microstructure observations is included in the next section.

4.3 Energy terms with distance from ridge

In this section we consider how the energy varies with distance from the ridge crest. As can be seen from Table 2, the baroclinic energy balance is predominately between three terms:

$$\nabla \cdot Flux \approx Conversion - Dissipation. \quad (7)$$

We integrate these terms over regions bounded by the 1000 m, 2000 m, and 3000 m isobaths, as well as lines paralleling the 3000 m isobath at distances of 10, 20, 30, 40, 60, 80, 100, and 120 km (Fig. 9a). Each region is further divided into north and south by a line that passes through the main islands (Fig. 9a, heavy line).

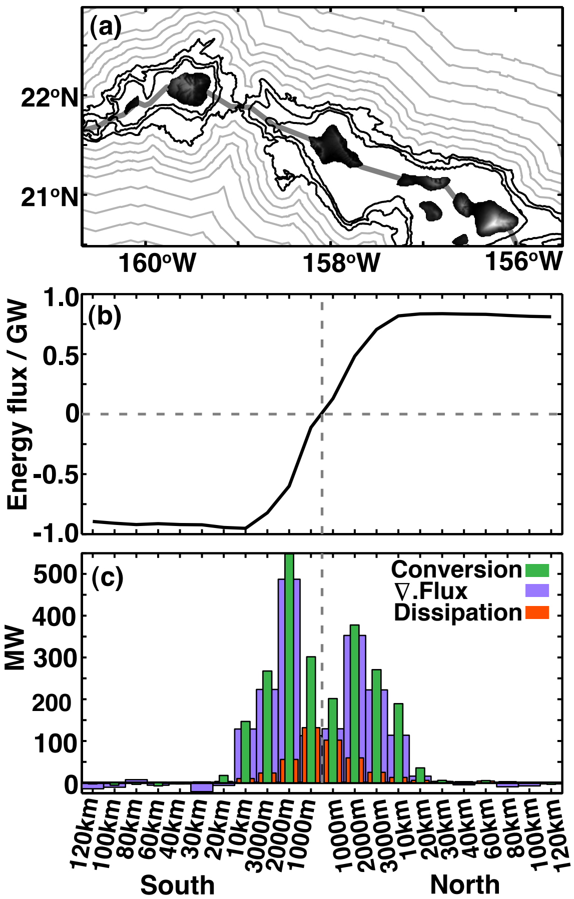

Figure 9: (a) Boundaries of the regions used for assessing the energy as a function of distance from the ridge crest. The lines are the 1000 m, 2000 m, and 3000 m isobaths, and lines paralleling the 3000 m isobath at distances of 10, 20, 30, 40, 60, 80, 100, and 120 km. The heavy line divides the regions into north and south. (b) Net baroclinic energy flux calculated by integrating flux divergence out to the lines given in the top panel. (c) Conversion, flux divergence and dissipation within the regions defined by the lines in the top panel.

The total southward flux peaks 10 km beyond the 3000 m isobath with a value of 0.95 GW (Fig. 9b). The northward flux is weaker (maximum of 0.84 GW) and peaks farther from the ridge, at a distance of 30 km from the 3000 m isobath. After peaking, the flux slowly decays with distance from the ridge. The flux 120 km from the 3000 m isobath is 3% (6%) lower than the maximum on the north (south) side of the ridge. However, it is not always possible to be within the model domain at 120 km from the 3000 m isobath (particularly south of the ridge), so, consequently, these flux decays are an overestimate.

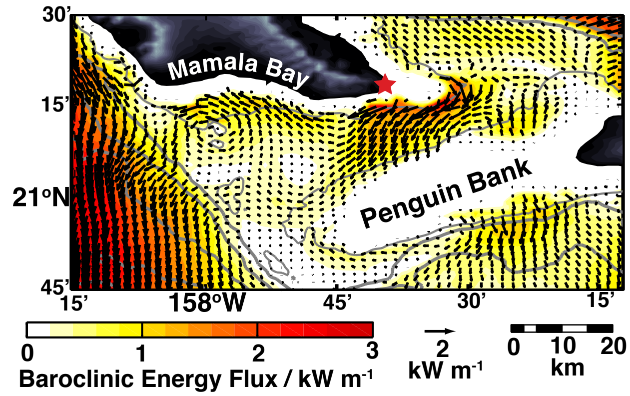

Figure 10: Depth-integrated M_2 baroclinic energy flux vectors for the region around Makapuu Point (marked with the red star). Every second vector in each direction has been plotted. The underlying color gives the flux magnitude. The line contours are at 500 m depth, and the thicker contours are at intervals of 1000 m.

The area-integrated conversion, baroclinic flux divergence and dissipation are all larger on the south side of the ridge (Fig. 9c). Most of the conversion (and flux divergence) occurs within 10 km of the 3000 m isobath, in agreement with the analysis presented in Fig. 6b. In most regions, the conversion is slightly larger than the flux divergence resulting in small dissipation. The exception is within the southern portion of the 1000 m isobath where the dissipation exceeds the flux divergence by 18.8 MW.

Thirty percent (132 MW out of 445 MW) of the total baroclinic dissipation in the model occurs within the 1000 m isobath south of the ridge crest. Of that 64.5 MW is dissipated between 158° 12′W and 157° 00′W, which encompasses Oahu minus Kaena Point through to the middle of Molokai. The majority of the relatively small amount of generation that occurs in this region is confined off Makapuu Point (Fig. 6a). The depth integrated flux vectors (Fig. 10) show that the internal tide generated at Makapuu point tends to either follow the coastline around into Mamala Bay (previously studied by Eich et al., 2004; Alford et al., 2006; Martini et al., 2007) or head south and be dissipated along the edge of Penguin Bank. In either case very little of the internal tide energy generated here crosses the 1000 m isobath. Not only does this contrast sharply with the majority of the generation sites where most of the energy radiates significant distances, but it means that 14% of the dissipation within the domain comes from a generation region with no radiative signature.

As part of the HOME Nearfield experiment, a total of 313 microstructure profiles were taken over topography

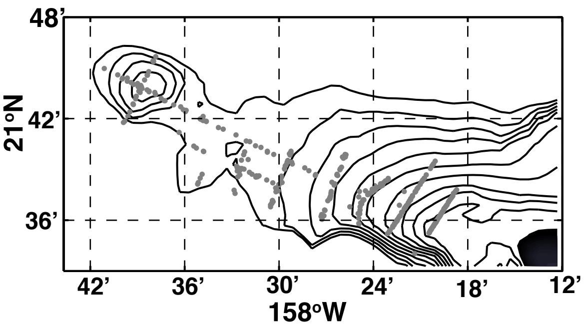

Figure 11: Location of AMP microstructure profiles taken over Kaena Ridge as part of the HOME Nearfield experiment. The contour interval is 100 m.

less than 1000 m deep on the Kaena Ridge (Fig. 11). The data were collected with the loosely tethered deep Advanced Microstructure Profiler (AMP), which evaluates ε from centimeter scale shear variance (Osborn and Crawford, 1980; Gregg, 1987; Wesson and Gregg, 1994). These data allow a comparison between the modeled baroclinic dissipation and field observations. The AMP profiles were integrated over the water column from 22 m depth (to avoid contamination from the ship) to $\sim$20 m above the bed (where profiling was stopped to avoid damaging the instrument on the rough volcanic seabed). The profiles were then binned according to bottom depth with a bin interval of 100 m, e.g., all profiles taken over topography between 100 and 200 m deep were grouped together. The profiles within each bin were then bootstrap averaged and multiplied by the area associated with that depth range (with the eastern boundary being 158° 12′). The area-integrated dissipation was 28 MW with a 95% confidence interval of [17 – 42] MW.

The modeled baroclinic dissipation within the 1000 m isobath for the Kaena Ridge west of 158° 12′ is 48.7 MW. This is above the upper limit of the 95% confidence interval on the area weighted observations, but is within a factor of 2 of the observed mean (28 MW). A factor of two is often taken as the threshold for determining equivalence between ε measurements (Osborn, 1980; Oakey, 1982; Carter and Gregg, 2002), so we, consider this acceptable agreement between the modeled dissipation and the microstructure. It should be noted that the microstructure observations include dissipation of energy from all sources, not just M_2 tides. However, M_2 is the dominant tidal frequency in this region, both in terms of barotropic velocity (Carter et al., 2006) and barotropic to baroclinic conversion (Zaron and Egbert, 2006a). The limited depth range used in the microstructure integration helps minimize the effect of surface and bottom boundary mixing on the comparison.

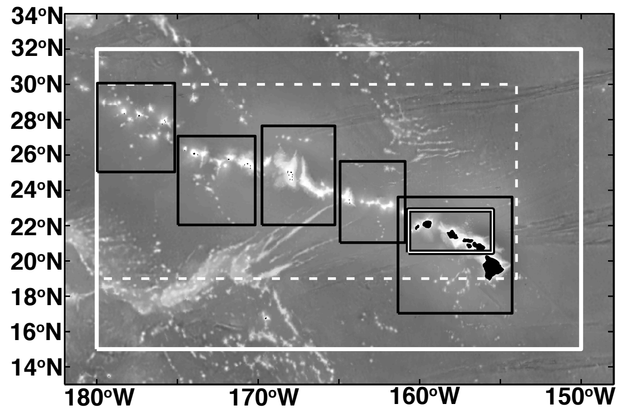

Figure 12: The extent of the current model domain compared to domains used in previous estimates of conversion at the Hawaiian Ridge. The current model is marked by the black-white-black line. The solid white line is used by Zaron and Egbert (2006a); the dashed line by Niwa and Hibiya (2001); and the solid black lines shows the five regions used in Merrifield and Holloway (2002), the regions were numbered from right to left.

5 Comparison to Merrifield and Holloway (2002)

The model results presented in Merrifield and Holloway (2002) were used extensively in both the planning and analysis of the HOME field observations (e.g., Rudnick et al., 2003; Klymak et al., 2006; Lee et al., 2006). They divided the Hawaiian Ridge into five subdomains (Fig. 12, black lines). Their simulations used 4 km resolution grids derived from Smith and Sandwell (1997) bathymetry, compared to the 0.01 degree ($\sim$1 km) multibeam derived grid used in the current analysis. In this section, we revisit some of the findings from Merrifield and Holloway (2002).

The small decrease in flux divergence that we find occurs off the ridge (Fig. 9b), contrasts with the $\sim$0.5 GW per 100 km decay rate reported by Merrifield and Holloway (2002). There appear to be two factors that contribute to their overestimate of energy flux decay. First, the integration time in their simulations was very short, only 4 days, which does not allow the higher modes to propagate throughout the domain. Carter and Merrifield (2007) plot energy flux from a ridge versus distance for a range of integration times, and the shape of the curves where the higher modes have not reach the boundary are similar to those shown by Merrifield and Holloway

(2002). Second, Merrifield and Holloway (2002) calculate the energy flux by 'integrating the ridge normal component of the energy flux density vector', i.e.,

$$f_1(x) = \int_{y_2}^{y_1} \vec{F}(x, y')dy', \tag{8}$$

where the domain has been rotated so the ridge lies in the x-direction. Unlike the area integral used in Fig. 9, this approach does not account for radial spreading and energy leaving through the side of the box.

The magnitude of modeled internal tide generation is sensitive to topographic resolution (Di Lorenzo et al., 2006; Zilberman et al., 2007). In particular, the barotropic to baroclinic conversion is reduced for a coarser grid, or when the underlying bathymetry is smoothed. To assess the effect of the higher resolution topography on generation around Hawaii, we conducted an 18 M_2 tidal cycle simulation using the same 4 km resolution, Smith and Sandwell (1997) topography derived, grid that Merrifield and Holloway (2002) used for their region 1. Equation (6) then gives the generation[3], over a subregion corresponding to the 0.01 degree domain, as 1.843 GW. This is 19–22% lower than the corresponding conversion values from Table 2 or from (6) applied to the current simulation. Limited computing resources do not allow us to run our domain at any finer resolution at this time, and therefore, we cannot be sure that $\sim$1 km resolution is sufficient for the internal tide generation to converge.

Merrifield and Holloway (2002) do not directly calculate internal tide generation, but rather they estimate it from integrating the flux divergence over regions shallower than 4000 m depth. This approach excludes baroclinic energy that is generated and dissipated within the integration region. Integrating the 4 km flux divergence over the region of the high resolution model gives 1.380 GW, i.e., Merrifield and Holloway (2002) underestimate generation by $\sim$40% compared to Table 2.

By assuming that the 4 km flux divergence underestimates the generation over the Hawaiian Ridge as it does between Niihau and Maui, it is possible to extrapolate our results to the entire Merrifield and Holloway (2002) domain. Scaling their estimated 10.2 GW up by 40% gives 14.3 GW of barotropic to baroclinic conversion. Niwa and Hibiya (2001) applied (6) to a 1/16° ($\sim$7 km) resolution primitive equation simulation, and found $\sim$15 GW of conversion for the region bounded by the white dashed line in Fig. 12. Recall that we found (6) applied to a 4 km resolution model underestimated conversion from (4) and (5) by $\sim$20%. Assuming that underestimation for the 1/16° resolution model is at least as large, then the revised conversion value would be $\gtrsim$18 GW. The difference between the estimates from extrapolating Merrifield and Holloway (2002) and Niwa and Hibiya (2001) may be due to different size domains, in particular conversion occurring in the gaps between the Merrifield and Holloway (2002) subdomains.

Zaron and Egbert (2006a) using a 2-D satellite altimetry constrained inverse model estimate 19 GW of M_2 barotropic flux divergence over the Hawaiian Ridge (Fig. 12, solid white line). Based on our findings (Table 2), 84% of this (16 GW) goes into internal tides. This lies between the scaled estimates of Merrifield and Holloway (2002) and Niwa and Hibiya (2001).

6 Summary and discussion

An one-hundredth of a degree horizontal resolution primitive equation (Princeton Ocean Model) simulation is used to derive a M_2 energy budget for the region from Niihau to Maui. This domain includes the Kaena Ridge, which had been previously identified as one of the main sites of barotropic to baroclinic conversion along the Hawaiian Ridge. The simulation was found to have a high level of skill when validated against satellite and in-situ sealevel observations, currents from moored ADCPs, and even microstructure measurements. RMS errors comparing the simulation to M_2 harmonic fits from data were $\lesssim$1 cm compared to sealevel, and $\sim$0.035 m s^{-1} for moored velocity observations. The modeled baroclinic dissipation (a combination of Mellor and Yamada vertical mixing and Smagorinsky horizontal diffusivity) agrees to within a factor of two with the area weighted integral of 313 microstructure profiles taken over the Kaena Ridge. To our knowledge, this is the most direct comparison of microstructure data to an internal tide process model yet.

Barotropic and baroclinic energy equations were derived from POM's governing equations. Of the 2.7 GW lost from the barotropic tide, 163 MW is dissipated by bottom friction and 2.3 GW is converted into internal tides. The majority of the internal tide energy (1.7 GW) is radiated out of the model domain, while 0.45 GW is dissipated close to the generation regions. Figure 13 gives a schematic summary of this M_2 energy pathway. Note that the 16% of the barotropic flux divergence that is lost to baroclinic dissipation compares well to the $\sim$15% found by Klymak et al. (2006) from an extrapolation of mi-

[3]Both the Merrifield and Holloway (2002) simulation and our rerun of that grid, contain significantly more cell-to-cell numerical noise than the $\sim$1 km simulation presented in this paper. This is primarily because of the different scales of the underlying datasets (Smith and Sandwell is much coarser than multibeam), and hence the 4 km grid can not be considered smoother than the current grid. This numerical noise affects the energy calculation of (4) and (5). The baroclinic conversion and dissipation terms were most effected by the noise. Consequently, we use (6) here to estimate the generation.

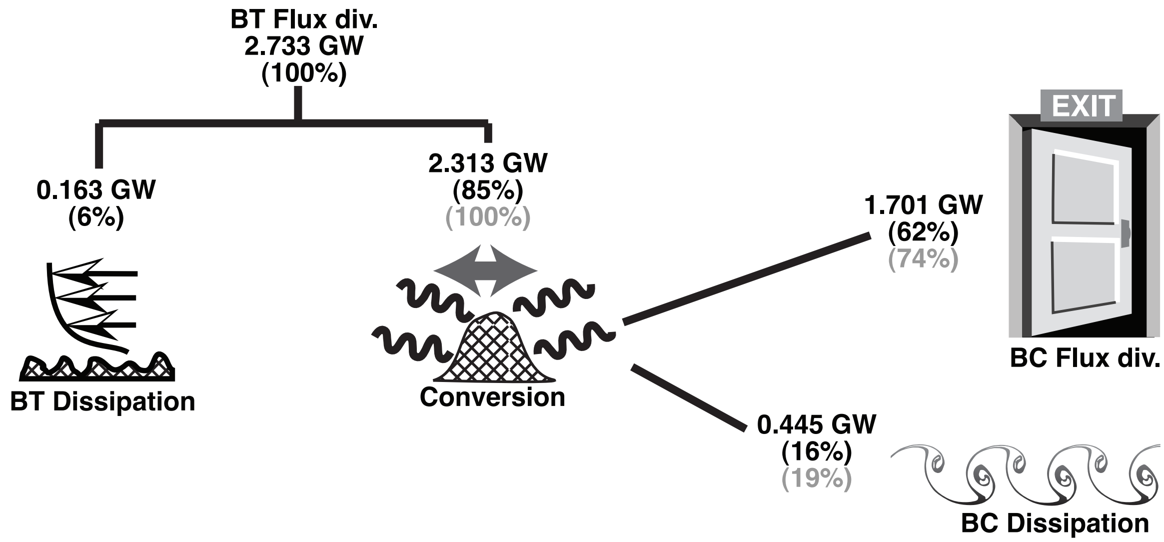

Figure 13: Cartoon summarizing the major components to the M$_2$ tidal energy budget in the model. The percentages given in black are relative to the energy lost from the barotropic tide, and those in gray are relative to the barotropic to baroclinic conversion. The conversion value used is the average of the two estimates in Table 2.

crostructure observations to the entire Hawaiian Ridge. The 74% of baroclinic energy radiated out of the domain is consistent with the analytical work of St. Laurent and Garrett (2002), who found that less than 30% of the energy flux is generated at smaller spatial scales and may be available to dissipate locally.

An interesting exception to the general rule that the vast majority of the baroclinic energy radiates away is that almost all of the internal tide generated at Makapuu (southeast tip of Oahu) is dissipated within the 1000 m isobath. This small generation site accounts for 14% of the baroclinic dissipation within the domain. We postulate that other such regions, where $local\ dissipation \approx conversion$, must exist in the global ocean, and hence may play a role in global energy budgets.

We find that by equating conversion to flux divergence at the 4000 m isobath and using Smith and Sandwell (1997) derived, 4 km resolution, topography, Merrifield and Holloway (2002) underestimated barotropic to baroclinic conversion by $\sim$40% compared to the 1 km resolution, multibeam derived, bathymetry used in the present study. Further, applying the energy equations (4) and (5) to the coarser Merrifield and Holloway (2002) model grid still underestimates conversion by $\sim$20% compared to our simulation. This indicates that a detailed energy budget for the entire Hawaiian Ridge will require multibeam derived bathymetry over a much larger area than currently available.

Acknowledgments

The bathymetry data were provided and gridded to 0.01° by Paul Johnson of the Hawaii Regional Mapping Group. We thank Jerome Aucan, Kevin Bartlett, Cedric Chavanne, Thomas Decloedt, Walt Waldorf, Nathalie Zilberman, and the crew of the R/V Wecoma for assistance with the mooring data. The microstructure data were collected with the assistance of Matthew Alford, Paul Aguilar, Steve Bayer, Earl Krause, John Mickett, Jack Miller, Avery Synder, Maya Whitmont, Dave Winkel, and the crew of the R/V Revelle. Richard Ray kindly provided the harmonic fits to the along track satellite data. The authors thank two anonymous reviewers.

This work was funded by the National Science Foundation (NSF) grant OCE0425347. The microstructure and moored current data employed in this paper were collected as part of the Hawaii Ocean Mixing Experiment. The microstructure data collection was supported by NSF grants OCE9818693 and OCE9819535 to M. Gregg and J. Miller at the University of Washington; the mooring data collection was supported by NSF grant OCE9819533 to D. Luther and M. Merrifield at the University of Hawaii, and grant OCE9819532 to M. Levine and T. Boyd at Oregon State University. The temperature and salinity data from Station ALOHA were supplied by the Hawaii Ocean Timeseries program (NSF grants OCE9303094, 0117919, and 0327513).

A Derivation of energy equations

Here we outline the derivation of the barotropic and baroclinic energy equations presented above. Using the definitions from Section 3, the hydrostatic and Boussinesq equations of motion in σ-coordinates are:

$$\frac{\partial u}{\partial t}+\mathcal{A}_x-fv=-g\frac{\partial\eta}{\partial x}-\frac{1}{\rho_0}\frac{\partial p}{\partial x}-\frac{\rho}{\rho_0}g\left(\sigma\frac{\partial D}{\partial x}+\frac{\partial\eta}{\partial x}\right)+\mathcal{D}_x+\mathcal{F}_x \quad \text{(A.1)}$$

$$\frac{\partial v}{\partial t}+\mathcal{A}_y+fu=-g\frac{\partial\eta}{\partial y}-\frac{1}{\rho_0}\frac{\partial p}{\partial y}-\frac{\rho}{\rho_0}g\left(\sigma\frac{\partial D}{\partial y}+\frac{\partial\eta}{\partial y}\right)+\mathcal{D}_y+\mathcal{F}_y \quad \text{(A.2)}$$

$$\frac{\partial\eta}{\partial t}+\frac{\partial(uD)}{\partial x}+\frac{\partial(vD)}{\partial y}+\frac{\partial\omega}{\partial\sigma}=0 \quad \text{(A.3)}$$

$$\frac{\partial\rho}{\partial t}+\mathcal{A}_\rho=-w\frac{\partial\hat{\rho}}{\partial z}+\mathcal{D}_\rho+\mathcal{F}_\rho \quad \text{(A.4)}$$

where the advection terms are

$$\mathcal{A}_x=\mathbf{u}\cdot\nabla u+\frac{\omega}{D}\frac{\partial u}{\partial\sigma} \quad \text{(A.5)}$$

$$\mathcal{A}_y=\mathbf{u}\cdot\nabla v+\frac{\omega}{D}\frac{\partial v}{\partial\sigma} \quad \text{(A.6)}$$

$$\mathcal{A}_\rho=\mathbf{u}\cdot\nabla\rho+\frac{\omega}{D}\frac{\partial\rho}{\partial\sigma}, \quad \text{(A.7)}$$

and the vertical and horizontal dissipative terms are

$$\mathcal{D}_x=\frac{1}{D}\frac{\partial}{\partial\sigma}\left(\frac{\kappa_m}{D}\frac{\partial u}{\partial\sigma}\right) \quad \text{(A.8)}$$

$$\mathcal{D}_y=\frac{1}{D}\frac{\partial}{\partial\sigma}\left(\frac{\kappa_m}{D}\frac{\partial v}{\partial\sigma}\right) \quad \text{(A.9)}$$

$$\mathcal{F}_x=\frac{1}{D}\left\{\frac{\partial}{\partial x}\left[2A_MH\frac{\partial u}{\partial x}\right]+\frac{\partial}{\partial y}\left[A_MH\left(\frac{\partial u}{\partial y}+\frac{\partial v}{\partial x}\right)\right]\right\} \quad \text{(A.10)}$$

$$\mathcal{F}_y=\frac{1}{D}\left\{\frac{\partial}{\partial x}\left[A_MH\left(\frac{\partial u}{\partial y}+\frac{\partial v}{\partial x}\right)\right]+\frac{\partial}{\partial y}\left[2A_MH\frac{\partial v}{\partial y}\right]\right\}. \quad \text{(A.11)}$$

A_M is the horizontal kinematic viscosity:

$$A_M=c\frac{\Delta x\Delta y}{2}\sqrt{\left(\frac{\partial u}{\partial x}\right)^2+\left(\frac{\partial v}{\partial x}+\frac{\partial u}{\partial y}\right)^2+\left(\frac{\partial v}{\partial y}\right)^2}, \quad \text{(A.12)}$$

and κ_m is the vertical eddy diffusivity from the Mellor and Yamada (1982) submodel. The surface and bottom boundary conditions on $\frac{\kappa_m}{D}\left(\frac{\partial u}{\partial\sigma},\frac{\partial v}{\partial\sigma}\right)$ are given by the surface wind stress and bottom frictional stress, respectively (Blumberg and Mellor, 1987). Finally, we do not provide explicit definitions of the vertical and horizontal dissipation terms ($\mathcal{D}_\rho$ and $\mathcal{F}_\rho$), as these terms are identically zero in our analysis because temperature and salinity are only advected.

For the barotropic energy equation, we recast the momentum equations [(A.1) and (A.2)] to take advantage of the pressure gradient variables calculated by the model (Blumberg and Mellor, 1987; Mellor, 2004):

$$\frac{\partial(uD)}{\partial t}+\frac{\partial(u^2D)}{\partial x}+\frac{\partial(uvD)}{\partial y}+\frac{\partial(u\omega)}{\partial\sigma}-fvD+gD\frac{\partial\eta}{\partial x}+D\frac{g}{\rho_0}\int_\sigma^0\left[D\frac{\partial\rho}{\partial x}-\sigma'\frac{\partial D}{\partial x}\frac{\partial\rho}{\partial\sigma'}\right]\mathrm{d}\sigma'=D\left(\mathcal{D}_x+\mathcal{F}_x\right) \quad \text{(A.13)}$$

$$\frac{\partial(vD)}{\partial t}+\frac{\partial(uvD)}{\partial x}+\frac{\partial(v^2D)}{\partial y}+\frac{\partial(v\omega)}{\partial\sigma}+fuD+gD\frac{\partial\eta}{\partial y}+D\frac{g}{\rho_0}\int_\sigma^0\left[D\frac{\partial\rho}{\partial y}-\sigma'\frac{\partial D}{\partial y}\frac{\partial\rho}{\partial\sigma'}\right]\mathrm{d}\sigma'=D\left(\mathcal{D}_y+\mathcal{F}_y\right) \quad \text{(A.14)}$$

We define the σ-averaged as

$$\overline{(\cdot)}\equiv\int_{-1}^0(\cdot)d\sigma.$$

The σ-averaged form of (A.13), denoted $\overline{(A.13)}$, then becomes

$$\frac{\partial\overline{u}}{\partial t}+\overline{\mathcal{A}'}_x-f\overline{v}=-g\frac{\partial\eta}{\partial x}-\overline{\frac{g}{\rho_0}\int_\sigma^0\left[D\frac{\partial\rho}{\partial x}-\sigma'\frac{\partial D}{\partial x}\frac{\partial\rho}{\partial\sigma'}\right]\mathrm{d}\sigma'}+\overline{\mathcal{D}_x}+\overline{\mathcal{F}_x},$$

where

$$\overline{\mathcal{A}'_x}=\overline{u}\frac{\partial\overline{u}}{\partial x}+\overline{v}\frac{\partial\overline{u}}{\partial y}+\frac{1}{D}\left\{\frac{\partial}{\partial x}\left[D\left(\overline{u^2}-\overline{u}^2\right)\right]+\frac{\partial}{\partial y}\left[D\left(\overline{uv}-\overline{u}\ \overline{v}\right)\right]\right\}.$$

The σ-averaged continuity equation, denoted $\overline{(A.3)}$, is

$$\frac{\partial \eta}{\partial t} + \frac{\partial \overline{u} D}{\partial x} + \frac{\partial \overline{v} D}{\partial y} = 0.$$

The barotropic energy equation (4) then is obtained by evaluating

$$D\overline{u} \times \overline{(A.13)} + D\overline{v} \times \overline{(A.14)} + \left(g\eta + \frac{\overline{p}}{\rho_0} \right) \times \overline{(A.3)}.$$

The baroclinic component is formed by subtracting the σ-average from (A.1) – (A.4). For example, $\widetilde{(A.1)} = (A.1) - \overline{(A.1)}$:

$$\frac{\partial \widetilde{u}}{\partial t} + \widetilde{\mathcal{A}_x} - f\widetilde{v} = -\frac{1}{\rho_0}\frac{\partial \widetilde{p}}{\partial x} - \frac{g}{\rho_0}\left(\widetilde{\rho\sigma}\frac{\partial D}{\partial x} + \widetilde{\rho}\frac{\partial \eta}{\partial x} \right) + \widetilde{\mathcal{D}_x} + \widetilde{\mathcal{F}_x},$$

noting that $\widetilde{\mathcal{A}_x} = \mathcal{A}_x - \overline{\mathcal{A}'_x}$. The continuity, $\widetilde{(A.3)}$, becomes

$$\frac{\partial}{\partial x}(\widetilde{u}D) + \frac{\partial}{\partial y}(\widetilde{v}D) + \frac{\partial \omega}{\partial \sigma} = 0.$$

The baroclinic energy equation obtained by evaluating

$$D\widetilde{u} \times \widetilde{(A.1)} + D\widetilde{v} \times \widetilde{(A.2)} + \frac{\widetilde{p}}{\rho_0} \times \widetilde{(A.3)} + Dg\frac{\rho}{\rho_0}\left(-\frac{\mathrm{d}\hat{\rho}}{\mathrm{d}z} \right)^{-1} \times (A.4)$$

must then be vertically integrated to give (5).

The Princeton Ocean Model uses a staggered (Arakawa C) grid in the horizontal, defines the across-sigma velocity and turbulence quantities on the σ-levels, and the horizontal velocity and density on the midpoint of the σ-levels (Blumberg and Mellor, 1987; Mellor, 2004). All the terms in (4) and (5) are evaluated on the horizontal and vertical midpoint of the grid cells.

References

Alford, M. H., M. Gregg, and M. A. Merrifield, 2006: Structure, propagation, and mixing of energetic baroclinic tides in Mamala Bay, Oahu, Hawaii. *Journal of Physical Oceanography*, **36**(6), 997–1018.

Aucan, J. and M. A. Merrifield, 2007: Boundary mixing associated with tidal and near-inertial internal waves. *Journal of Physical Oceanography*, **Accepted**.

Aucan, J., M. A. Merrifield, D. S. Luther, and P. Flament, 2006: Tidal mixing events on the deep flanks of Kaena Ridge, Hawaii. *Journal of Physical Oceanography*, **36**(6), 1202–1219.

Balmforth, N. J., G. R. Ierley, and W. R. Young, 2002: Tidal conversion by subcritical topography. *Journal of Physical Oceanography*, **32**, 2900–2914.

Blumberg, A. F. and G. L. Mellor, 1987: A description of a three-dimensional ocoastal ocean circulation model. In N. S. Heaps, editor, *Three-dimensional coastal ocean models*, Coastal and Estuarine Sciences 4, 1–16, American Geophysical Union, Washington, D. C.

Carter, G. S. and M. C. Gregg, 2002: Intense, variable mixing near the head of Monterey Submarine Canyon. *Journal of Physical Oceanography*, **32**(11), 3145–3165.

Carter, G. S. and M. C. Gregg, 2006: Persistent near-diurnal internal waves observed above a site of M_2 barotropic-to-baroclinic conversion. *Journal of Physical Oceanography*, **32**(6), 1136–1147.

Carter, G. S., M. C. Gregg, and M. A. Merrifield, 2006: Flow and mixing around a small seamount on Kaena Ridge, Hawaii. *Journal of Physical Oceanography*, **36**(6), 1036–1052.

Carter, G. S. and M. A. Merrifield, 2007: Open boundary conditions for regional tidal simulations. *Ocean Modelling*, **18**, 194–209.

Chavanne, C., 2007: *Observations of the Impact of Mesoscale Currents on Internal Tide Propagation*. Ph.D. thesis, University of Hawai'i.

Chiswell, S. M., 1994: Vertical structure of the baroclinic tides in the central North Pacific subtropical gyre. *Journal of Physical Oceanography*, **24**(9), 2032–2039.

Cummins, P. F. and L.-Y. Oey, 1997: Simulation of barotropic and baroclinic tides off Northern British Columbia. *Journal of Physical Oceanography*, **27**(5), 762–781.

Di Lorenzo, E., W. R. Young, and S. Llewellyn Smith, 2006: Numerical and analytical estimates of m_2 tidal conversion at steep oceanic ridges. *Journal of Physical Oceanography*, **36**(6), 1072–1084.

Dushaw, B. D., B. D. Cornuelle, P. F. Worcester, B. M. Howe, and D. S. Luther, 1995: Barotropic and baroclinic tides in the Central North Pacific Ocean determined from long-range reciprocal acoustic transmissions. *Journal of Physical Oceanography*, **25**(4), 631–647.

Egbert, G. D., 1997: Tidal data inversion: Interpolation and inference. *Progress in Oceanography*, **40**, 53–80.

Egbert, G. D. and S. Y. Erofeeva, 2002: Efficient inverse modeling of barotropic ocean tides. *Journal of Atmospheric and Oceanic Technology*, **19**(2), 183–204.

Egbert, G. D. and R. D. Ray, 2000: Significant dissipation of tidal energy in the deep ocean inferred from satellite altimeter data. *Nature*, **405**, 775–778.

Egbert, G. D. and R. D. Ray, 2001: Esitimates of M_2 tidal energy dissipation from TOPEX/Poseidon altmeter data. *Journal of Geophysical Research*, **106**(C10), 22,475–22,502.

Eich, M. L., M. A. Merrifield, and M. Alford, 2004: Structure and variability of semidiurnal internal tides in Mamala Bay, Hawaii. *Journal of Geophysical Research*, **109**, C05010,doi:10.1029/2003JC002049.

Flather, R. A., 1976: A tidal model of the north-west European continental shelf. *Memoires de la Societe Royale des Sciences de Liege*, **6**(10), 141–164.

Garrett, C. and E. Kunze, 2007: Internal tide generation in the deep ocean. *Annual Review of Fluid Mechanics*, **39**, 57–87.

Gregg, M. C., 1987: Diapycnal mixing in the thermocline: a review. *Journal of Geophysical Research*, **92**(C5), 5249–5286.

Hodges, B. R., B. Laval, and B. M. Wadzuk, 2006: Numerical error assessment and a temporal horizon for internal waves in a hydrostatic model. *Ocean Modelling*, **13**, 44–46.

Holloway, P. E. and M. A. Merrifield, 1999: Internal tide generation by seamounts, ridges, and islands. *Journal of Geophysical Research*, **104**(C11), 25,937–25,951.

Holloway, P. E., E. Pelinovsky, and T. Talipova, 1999: Modeling internal tide generation and evolution into internal solitary waves on the Australian North West Shelf. In P. Müller and D. Henderson, editors, *Dynamics of oceanic internal gravity waves II, Proceedings of the 'Aha Huliko'a Hawaiian Winter Workshop*, 43–49, University of Hawaii at Manoa.

Johnston, T. M. S. and M. A. Merrifield, 2003: Internal tide scattering at seamounts, ridges, and islands. *Journal of Geophysical Research*, **108**(C6), 3180, doi:10.1029/2002JC001528.

Johnston, T. M. S., M. A. Merrifield, and P. E. Holloway, 2003: Internal tide scattering at the Line Islands. *Journal of Geophysical Research*, **108**(C11), 3365, doi:10.1029/2003JC001844.

Kang, S. K., M. G. G. Foreman, W. R. Crawford, and J. Y. Cherniawsky, 2000: Numerical modeling of internal tide generation along the Hawaiian Ridge. *Journal of Physical Oceanography*, **30**(5), 1083–1098.

Katsumata, K., 2006: Tidal stirring and mixing on the Australian North West shelf. *Marine and Freshwater Research*, **57**(3), 243–254.

Klymak, J. M., J. N. Moum, J. D. Nash, E. Kunze, J. B. Girton, G. S. Carter, C. Lee, T. B. Sanford, and M. C. Gregg, 2006: An estimate of energy lost to turbulence at the Hawaiian Ridge. *Journal of Physical Oceanography*, **36**(6), 1148–1164.

Kunze, E., L. K. Rosenfeld, G. S. Carter, and M. C. Gregg, 2002: Internal waves in Monterey Submarine Canyon. *Journal of Physical Oceanography*, **32**(6), 1890–1913.

Lamb, K. G., 2004: Nonlinear interaction among internal wave beams generated by tidal flow over supercritical topography. *Geophysical Research Letters*, **31**, L09313, doi:10.1029/2003GL019393.

Larson, J. C., 1977: Cotidal charts for the Pacific Ocean near Hawaii using f-plane solutions. *Journal of Physical Oceanography*, **7**(1), 100–109.

Lee, C. M., E. Kunze, T. B. Sanford, J. D. Nash, M. A. Merrifield, and P. E. Holloway, 2006: Internal tides and turbulence along the 3000-m isobath of the Hawaiian Ridge. *Journal of Physical Oceanography*, **36**(6), 1165–1183.

Mahadevan, A., 2006: Modeling vertical motion at ocean fronts: Are nonhydrostatic effects relevant at submesoscales? *Ocean Modelling*, **14**, 222–240.

Martini, K. I., M. H. Alford, J. Nash, E. Kunze, and M. A. Merrifield, 2007: Diagnosing a standing wave in Mamala Bay, Oahu. *Geophysical Research Letters*, **34**, L17604, doi:10.1029/2007GL029749.

Mellor, G. L., 2004: *User's guide for a three-dimensional, primitive equation, numerical ocean model*. Program in Atmospheric and Oceanic Sciences, Princeton University, Princeton, NJ 08544-0710.

Mellor, G. L., T. Ezer, and L.-Y. Oey, 1994: The pressure gradient conundrum of sigma coordinate ocean models. *Journal of Atmospheric and Oceanic Technology*, **11**(8), 1126–1134.

Mellor, G. L. and T. Yamada, 1982: Development of a turbulence closure model for geophysical fluid problems. *Reviews of geophysics and space physics*, **20**(4), 851–875.

Merrifield, M. A. and P. E. Holloway, 2002: Model estimates of M_2 internal tide energetics at the Hawaiian Ridge. *Journal of Geophysical Research*, **107**(C8), 10.1029/2001JC000996.

Merrifield, M. A., P. E. Holloway, and T. M. S. Johnston, 2001: The generation of internal tides at the Hawaiian Ridge. *Geophysical Research Letters*, **28**(4), 559–562.

Nash, J. D., E. Kunze, C. M. Lee, and T. B. Sanford, 2006: Structure of the baroclinic tide generated at Kaena Ridge, Hawaii. *Journal of Physical Oceanography*, **36**(6), 1123–1135.

Niwa, Y. and T. Hibiya, 2001: Numerical study of the spatial distribution of the M_2 internal tide in the Pacific Ocean. *Journal of Geophysical Research*, **106**(C10), 22,441–22,449.

Oakey, N. S., 1982: Determination of the rate of dissipation of turbulent energy from simultaneous temperature and velocity shear microstructure measurements. *Journal of Physical Oceanography*, **12**, 256–271.

Osborn, T. R., 1980: Estimates of the local rate of vertical diffusion from dissipation measurements. *Journal of Physical Oceanography*, **10**, 83–89.

Osborn, T. R. and W. R. Crawford, 1980: An airfoil probe for measuring turbulent velocity fluctuations in water. In F. Dobson, L. Hasse, and R. Davis, editors, *Air-Sea interaction: Instruments and Methods*, 369–386, Plenum Press.

Pinkel, R. and D. Rudnick, 2006: Editorial. *Journal of Physical Oceanography*, **36**(6), 965–966.

Rattray, M., J. G. Dworski, and P. E. Kovala, 1969: Generation of long internal waves at the continental slope. *Fuglister Sixtieth Anniversary Volume, Deep Sea Research*, **16**(Supplement), 179–195.

Ray, R. D. and G. T. Mitchum, 1996: Surface manifestation of internal tides generated near Hawaii. *Geophysical Research Letters*, **23**, 2101–2104.

Ray, R. D. and G. T. Mitchum, 1997: Surface manifestation of internal tides in the deep ocean: Observations from altimetry and island gauges. *Progress in Oceanography*, **40**, 135–162.

Rudnick, D. L., T. J. Boyd, R. E. Brainard, G. S. Carter, G. D. Egbert, M. C. Gregg, P. E. Holloway, J. M. Klymak, E. Kunze, C. M. Lee, M. D. Levine, D. S. Luther, J. P. Martin, M. A. Merrifield, J. N. Moum, J. D. Nash, R. Pinkel, L. Rainville, and T. B. Sanford, 2003: From tides to mixing along the Hawaiian Ridge. *Science*, **301**, 355–357.

Simmons, H. L., R. W. Hallberg, and B. K. Arbic, 2004: Internal wave generation in a global baroclinic tide model. *Deep-Sea Research II*, **51**(25–26), 3043–3068.

Smith, W. H. F. and D. T. Sandwell, 1997: Global seafloor topography from satellite altimetry and ship depth soundings. *Science*, **277**, 1956–1962.

St. Laurent, L. and C. Garrett, 2002: The role of internal tides in mixing the deep ocean. *Journal of Physical Oceanography*, **32**(10), 2882–2899.

Venayagamoorthy, S. K. and O. B. Fringer, 2005: Nonhydrostatic and nonlinear contributions to the energy flux budget in nonlinear internal waves. *Geophysical Research Letters*, **32**, L15603, doi:10.1029/2005GL023432.

Warner, J. C., C. R. Sherwood, H. G. Arango, and R. P. Signell, 2005: Performance of four turbulence closure models implemented using a generic length scale method. *Ocean Modelling*, **8**, 81–113.

Wesson, J. C. and M. C. Gregg, 1994: Mixing at Camarinal Sill in the Strait of Gibraltar. *Journal of Geophysical Research*, **99**, 9847–9878.

Zaron, E. D. and G. D. Egbert, 2006a: Estimating open-ocean barotropic tidal dissipation: The Hawaiian Ridge. *Journal of Physical Oceanography*, **36**(6), 1019–1035.

Zaron, E. D. and G. D. Egbert, 2006b: Verification studies for a z-coordinate primitive-equation model: Tidal conversion at a mid-ocean ridge. *Ocean Modelling*, **14**, 257–278.

Zilberman, N. V., M. A. Merrifield, and G. S. Carter, 2007: Internal tide generation over Mid-Atlantic Ridge topography. *Journal of Physical Oceanography*, **In Prep.**